Pathological responses to single pulse electrical stimuli in epilepsy: the role of feedforward inhibition

Supplementary material 1: Detailed model description, additional bifurcation analysis and supplementary data

Jurgen Hebbink[1,2], Geertjan Huiskamp[1], Stephan A. van Gils[2], Frans S.S. Leijten[1] and Hil G.E. Meijer[2]

[1]Department of Neurology and Neurosurgery, Brain Center Rudolf Magnus, University Medical Centre Utrecht, Heidelberglaan 100, 3584 CX Utrecht, The Netherlands
[2]Department of Applied Mathematics, MIRA Institute for Biomedical Engineering and Technical Medicine, University of Twente, Drienerlolaan 5, 7500 AE Enschede, The Netherlands

June 23, 2019

1 Introduction

In this supplementary material we give a detailed description of the extended Wendling neural mass model. Next, we perform bifurcation analysis with respect to the input parameter I in more detail and in a larger range than in the main text. Further, we perform a two parameter bifurcation analysis in C and I. Finally, we show the distribution of DR onset times for the remaining patients.

2 Detailed model description

In this section we describe the system of differential equations governing the dynamics of the extended Wendling model. This model consists of four neuronal populations. Before we derive the equations for the full neural mass, we first discuss the general principle for a single population of a neural mass model.

Figure 1A shows an overview of a single population. Each population has a mean membrane potential u, acting as the state variable of the population. The mean membrane potential is influenced by external inputs, i.e. activity from other populations either inside or outside the same neural mass. The inputs to a population are average firing rates and can be either excitatory $(z_{e,1}, \ldots, z_{e,N_e})$ or inhibitory $(z_{i,1}, \ldots, z_{i,N_i})$. Average firing rates $z_{e,k}$ (or $z_{i,k}$) are converted to postsynaptic potentials (PSPs) $x_{e,k}$ ($x_{i,k}$) via a second-order linear differential equation:

$$\ddot{x}(t) = Qqz(t) - 2q\dot{x}(t) - q^2x(t).$$

This differential equation is characterized by its impulse response function h:

$$h(t) = \begin{cases} Qqte^{-qt} & t \geq 0, \\ 0 & t < 0, \end{cases}$$

with $1/q$ the rising time of the synapse, i.e. the time after which the impulse response reaches its maximum, and Q the synaptic gain, regulating the magnitude of h. We distinguish three types of PSP transformations: one excitatory, modeling inputs from pyramidal and excitatory cells, and two inhibitory ones, modeling input from fast and slow inhibitory populations. Impulse responses of these PSP transformations are shown in Figure 4c of the main text, while their parameter values are given in Table 1.

The mean membrane potential of a population is obtained by multiplying each PSP by a connectivity constant and then adding up all excitatory PSPs and subtracting all inhibitory ones, i.e.

$$u = \sum_{k=1}^{N_e} C_{e,k} x_{e,k} - \sum_{k=1}^{N_i} C_{i,k} x_{i,k}.$$

Finally, the activity of a population, serving as input for other populations, is determined via the firing function S. This sigmoidal function is given by:

$$S(v) = \frac{2e_0}{1 + e^{r(v_0 - v)}} - \frac{2e_0}{1 + e^{rv_0}}.$$

A graph of this function is shown in Figure 4b of the main text. The parameters r, e_0, and v_0 influence the steepness, the magnitude, and the location of the median firing rate of the sigmoid function respectively. Their values are given in Table 1. Note that, in contrast to the original Wendling model [6], we shifted the sigmoid function such that $S(0) = 0$ and hence, firing rates should be interpreted as deviations from baseline.

Differential equations for the extended Wendling neural mass are obtained by coupling four populations as shown in Figure 1B. For a neural mass j we obtain the following set of differential equations:

$$\ddot{x}_1^{(j)} = AaS\big(u_{py}^{(j)}\big) - 2a\dot{x}_1^{(j)} - a^2 x_1^{(j)}, \tag{1a}$$
$$\ddot{x}_2^{(j)} = AaS\big(u_{ex}^{(j)}\big) - 2a\dot{x}_2^{(j)} - a^2 x_2^{(j)}, \tag{1b}$$
$$\ddot{x}_3^{(j)} = BbS\Big(u_{is}^{(j)}\Big) - 2b\dot{x}_3^{(j)} - b^2 x_3^{(j)}, \tag{1c}$$
$$\ddot{x}_4^{(j)} = GgS\Big(u_{if}^{(j)}\Big) - 2g\dot{x}_4^{(j)} - g^2 x_4^{(j)} \tag{1d}$$
$$\ddot{x}_5^{(j)} = AaI^{(j)} - 2a\dot{x}_5^{(j)} - a^2 x_5^{(j)}. \tag{1e}$$

The first four equations model the PSPs due to input from the pyramidal, excitatory, slow and fast inhibitory cells, respectively, while the last equation accounts for the external input $I^{(j)}$ to the neural mass. The potentials of the populations are given by:

$$u_{py}^{(j)} = C_2^{(j)} x_2^{(j)} - C_4^{(j)} x_3^{(j)} - C_7^{(j)} x_4^{(j)} + x_5^{(j)}, \tag{2a}$$
$$u_{ex}^{(j)} = C_1^{(j)} x_1^{(j)}, \tag{2b}$$
$$u_{is}^{(j)} = C_3^{(j)} x_1^{(j)} + \beta x_5^{(j)}, \tag{2c}$$
$$u_{if}^{(j)} = C_5^{(j)} x_1^{(j)} - C_6^{(j)} x_3^{(j)} + \gamma x_5^{(j)}. \tag{2d}$$

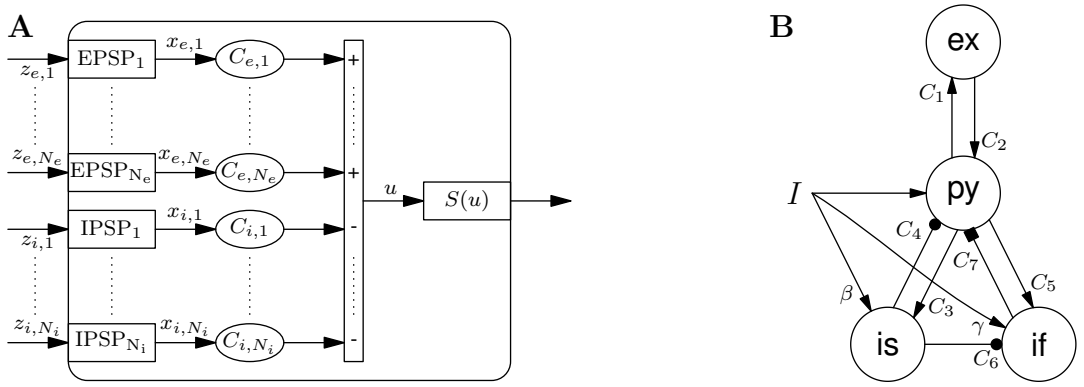

Figure 1: (**A**) Schematic overview of a single population. Each population may receive multiple excitatory inputs, labeled $z_{e,k}$, and inhibitory inputs, labeled $z_{i,k}$. These inputs are converted to the corresponding postsynaptic potentials $x_{e,k}$ and $x_{i,k}$. After multiplying by a connectivity constant excitatory PSPs are added and inhibitory ones subtracted resulting in the average membrane potential u. The activity of the population, serving as input for other populations, is obtained by applying a sigmoid function S to u. (**B**) Architecture of a single neural mass. The circles represent the four populations, i.e. pyramidal cells (py), local excitatory cells (ex), slow inhibitory cells (is) and fast inhibitory cells (if). Arrows represent excitatory connections, circles and squares are slow and fast inhibitory connections. Labels along the connections indicate connection strengths.

Constants $C_l^{(j)}$ denote the connectivity strengths, defined as $c_l C^{(j)}$, with $C^{(j)}$ an overall internal connectivity constant and c_l a scaling factor. We set the constants c_l to the same values as used by [6], see Table 1. In the first part we set $C^{(j)}$ to the same value as for the standard Wendling model. For the bifurcation analysis we vary $C^{(j)}$ as it resembles the excitability of the neural mass. The factors β and γ in the equations for u_{is} and u_{if}, are the fraction of the external input added to the slow and fast inhibitory cells, respectively.

The external input to a neural mass consists of three parts. First, the neural mass receives input from other neural masses. This input depends on the activity of the pyramidal cells and is given by:

$$k \sum_{l=1}^{N} M_{j,l} S\big(u_{py}^{(l)}\big),$$

Here, k is the overall connectivity strength and M the coupling matrix, with $M_{j,l}$ the connection strength from neural mass l to j. In this work, M is a 2×2 matrix with $M_{2,1} = 1$ and all other entries 0, as we only consider two feed-forward coupled neural masses. Second, the neural mass receives background input modeled as zero-mean Gaussian white noise with standard deviation σ. Finally, a neural mass may receive input due to single pulse electrical stimulation (SPES), which is modeled as a block pulse with an amplitude $P_0 = 1500$ and a duration of 5 ms. As explained in the main text multiple neural masses can receive this input at the same time as we assume that SPES activates the outgoing fibers of a stimulated region [1, 4].

In total we have a system of ten second-order differential equations. Solutions to these Itô-type stochastic differential equations are computed using an Euler-Maruyama scheme with fixed time steps of 0.1 milliseconds.

Parameter	Description	Value
A	Excitatory synaptic gain	4.5 mV
B	Slow inhibitory synaptic gain	7 mV
G	Fast inhibitory synaptic gain	25 mV
a	Reciprocal of excitatory time constant	100 s^{-1}
b	Reciprocal of slow inhibitory time constant	10 s^{-1}
g	Reciprocal of fast inhibitory time constant	300 s^{-1}
C	Internal connectivity constant	135
c_1	Relative conn. strength pyramidal to excitatory cells	1
c_2	Relative conn. strength excitatory to pyramidal cells	0.8
c_3	Relative conn. strength pyramidal to slow inhibitory cells	0.25
c_4	Relative conn. strength slow inhibitory to pyramidal cells	0.25
c_5	Relative conn. strength pyramidal to fast inhibitory cells	0.3
c_6	Relative conn. strength slow to fast inhibitory cells	0.1
c_7	Relative conn. strength fast inhibitory to pyramidal cells	0.8
σ	Standard deviation of noise	0 or 1 s^{-1}
k	Coupling strength between neural masses	varied
β	Scaling constant for external input to slow inhibitory cells	1
γ	Scaling constant for external input to fast inhibitory cells	0.7
e_0	Half of difference between min and max of the sigmoid function	2.5 s^{-1}
v_0	Potential for which the sigmoid function has its median value	4.5 mV
r	Steepness of sigmoid function	0.56 mV^{-1}

Table 1: Parameters for the neural mass model and their default values.

3 The effect of adding input to excitatory cells

External input in the model projects to the pyramidal cells as well as the two inhibitory populations. Here we investigate the influence of additional input to the local excitatory cells. Similarly as for the two inhibitory populations, we project the external input to the neural mass also onto the excitatory interneuron population in a proportional manner using a scaling constant α. Figure 2A shows the effect of increasing α on the ER. If the projection to the excitatory population is not too strong, i.e. $\alpha \leq 0.6$, the change in waveform of the early response is minimal. Only the amplitudes of the N1 and P1 peaks are affected, in a linear fashion. For $\alpha > 0.6$, nonlinear effects come into play, which can be counterbalanced by increasing values for the internal inhibitory coupling (not shown). Next, the effect of α on the DRs is shown in Figures 2B and C for $k = 30$ and $k = 100$. For $k = 30$ a DR is evoked for $\alpha \leq 0.2$. By increasing the coupling strength k DRs can also be found for $\alpha \leq 0.4$. These simulations show that adding feedforward input to the local excitatory cells does not quantitatively change our results, provided it is not too strong. Therefore, we ignore the feedforward excitation in the main text.

4 One parameter bifurcation diagram

In the main text we show the relevant bifurcations for modeling delayed responses (DRs), here we study the bifurcation diagram varying I in more detail. Bifurcation analysis is performed numerically using MatCont [2]. The resulting bifurcation diagram is shown in

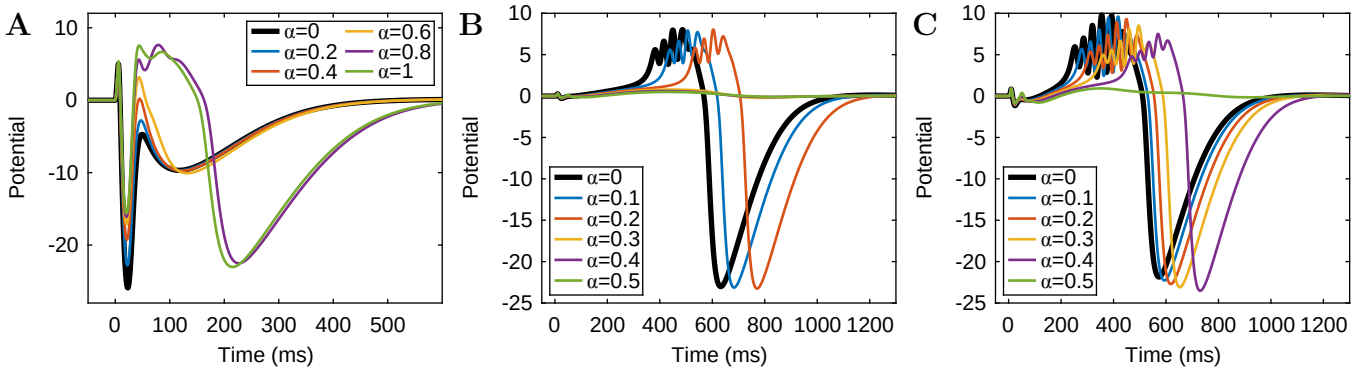

Figure 2: Effect of α on simulated responses. (**A**) Simulated ERs for various values of α. (**B**, **C**) Simulated DRs for $k = 30$ and $k = 100$, respectively.

Figure 3A. Starting from the stable equilibrium at $I = 0$ and continuing the equilibrium curve for negative values of I we find a Hopf bifurcation [5] at $I \approx -5.46$, two fold bifurcations [5] at $I \approx 5.58$ and $I = 14.2$ respectively, and another Hopf bifurcation at $I \approx -24.05$. Between the two Hopf bifurcations the equilibrium is unstable, with an unstable manifold of dimension one between the two fold bifurcations and two otherwise. Both for large positive and negative values of I the equilibrium undergoes two additional fold bifurcations (not shown).

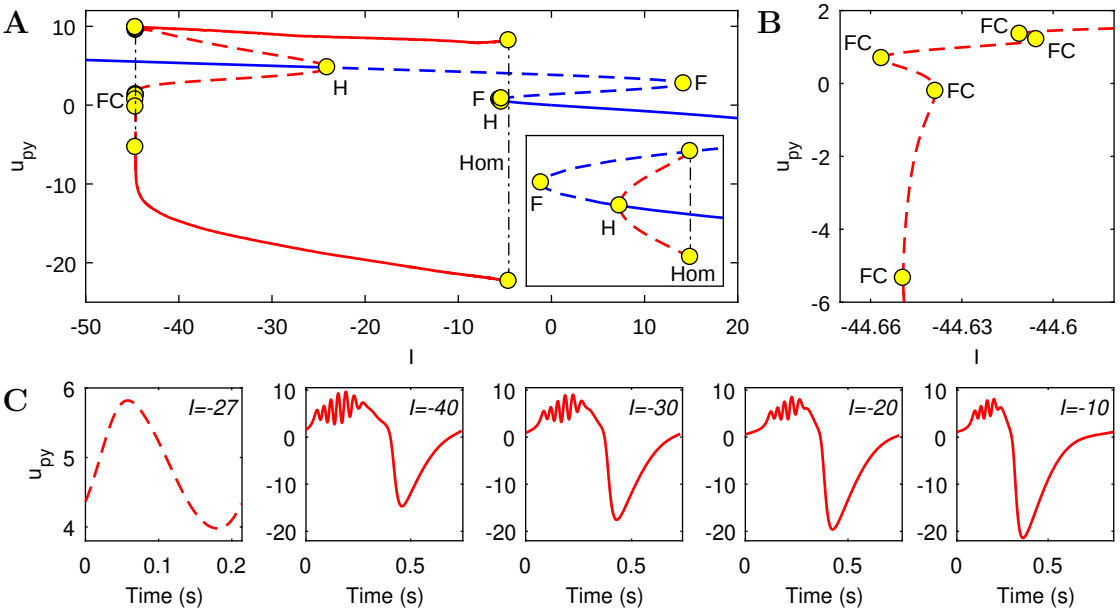

Figure 3: (**A**) Extended bifurcation diagram. Blue and red lines indicate equilibria and, minimum and maximum of limit cycles respectively. Solid lines and dashed lines represent stable and unstable solutions respectively. Fold (F), Hopf (H), fold of cycles (FC) and, saddle homoclinic (Hom) bifurcations are highlighted by yellow circles. The inset shows a magnification around the Hopf and fold bifurcations occurring near $I = 5$. (**B**) Close-up of **A** showing the minimum of the limit cycle around the fold of cycle bifurcations. (**C**) Time profiles of the limit cycle. Left profile shows the unstable limit cycle at $I = -27$, shortly after the Hopf bifurcation. Other profiles show the stable limit cycle for $I = -40$, -30, -20 and -10 respectively.

From the first Hopf bifurcation an unstable limit cycle emerges. This limit cycle exists only in a small range of I values and vanishes via a saddle homoclinic bifurcation (see [5]). More interesting is the unstable limit cycle emerging from the second Hopf bifurcation, which starts as an oscillation with a frequency of about 5 Hz (Figure 3C). Around $I = 44.6$ this limit cycle undergoes several fold of cycles bifurcations (see Figure 3B), while its minimum decreases rapidly. After the last fold of cycles bifurcation the limit cycle is stable and has also reached the characteristic form of a DR, i.e. some fast oscillations followed by the slow wave, with a period of around 0.75 s. This shape persists along the stable branch of the limit cycle curve (see Figure 3C). The period stays approximately constant till $I \approx 10$ and then increases rapidly. Finally, the limit cycle disappears via a saddle homoclinic bifurcation near $I \approx -4.58$. Note that there is bistability, i.e. both the stable limit cycle and the stable equilibrium exist, for I between -5.46 and -4.58.

5 Two parameter bifurcation diagram

So far we performed bifurcation analysis in one parameter, i.e. I, which revealed fold, Hopf and saddle homoclinic bifurcations. As discussed in the main text the first Hopf bifurcation is important as here the equilibrium loses stability. The same holds for the homoclinic bifurcation were the stable limit cycle vanishes. We now study how these bifurcation points changes in both I and C.

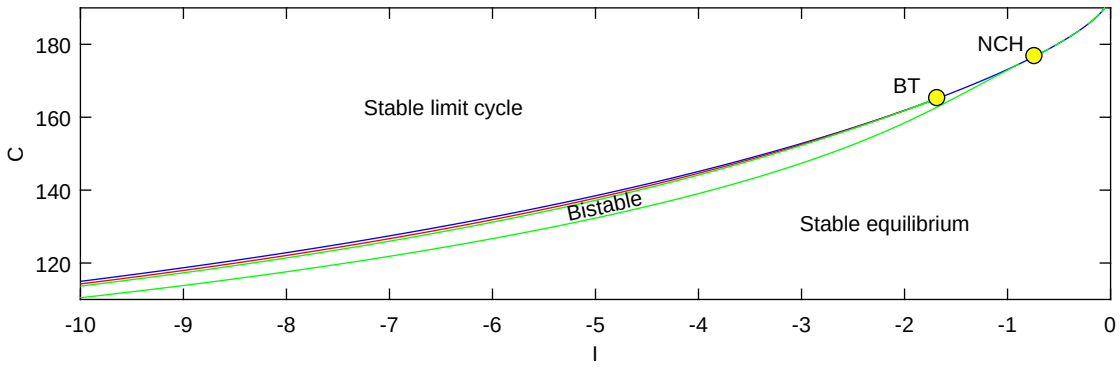

Figure 4: Bifurcation diagram in I and C. Blue line: fold bifurcation, red line: Hopf bifurcation, green lines: homoclinic bifurcation, dashed blue-green line: saddle-node homoclinic bifurcation.

Figure 4 shows the bifurcation diagram in I and C. The curves in this diagram show how the fold, Hopf, and homoclinic bifurcations vary with I and C. Four lines pass through $C = 135$, which represent from left to right the fold bifurcation (blue), Hopf bifurcation (red), homoclinic bifurcation of the unstable limit cycle (green) and the homoclinic bifurcation of the stable limit cycle (also green). To the right of the Hopf curve a stable equilibrium exists, while the stable limit cycle is present to the left of the right homoclinic curve. Note that there is a small area in which the system is bistable, i.e. both a stable equilibrium and limit cycle exist.

At $I \approx -1.68$ and $C \approx 165.2$ a Bogdanov-Takens bifurcation occurs and the Hopf and homoclinic curves terminate at the fold curve [5]. For larger values of C, the equilibrium loses stability at the fold curve. The fold curve and the remaining saddle homoclinic curve

meet at the non-central homoclinic saddle-node bifurcation (NCH) located at $I \approx -0.74$ and $C \approx 176.7$ [3]. Here, the saddle homoclinic curve ends and the fold curve turns into a saddle-node homoclinic curve [5] (dashed blue-green line). At the saddle-node homoclinic curve the limit cycle vanishes and simultaneously the equilibrium loses stability.

From the bifurcation diagram it follows that the proposed mechanism underlying DRs is robust with respect to C. If the input I is temporarily lowered enough then the stable equilibrium loses stability via either a Hopf, fold or saddle-node homoclinic bifurcation and the neural mass follows the stable limit cycle for about one period. While the input returns to zero the stable limit cycle vanishes via a homoclinic bifurcation (either a saddle homoclinic or a saddle-node homoclinic) and the neural mass will return to the equilibrium state. Moreover, for a higher intrinsic excitability C, these bifurcations occur for values of I closer to zero, implying that DRs can be generated using a smaller input deviation. As the deviation of the input increases with the connectivity strength k, this notion agrees with the results in Figure 8 of the main text, which shows that DRs occur for a smaller connectivity strength k if the excitability is higher.

6 Histograms DR onset times

Figures 5 and 6 show histograms with the distribution of the onset time of DRs for patients 1 and 3-11. Onset times of DRs is significantly later for DRs preceded by an ER compared to those that are not for patients 2-8 and 11, although the distributions have a large overlap in most patients.

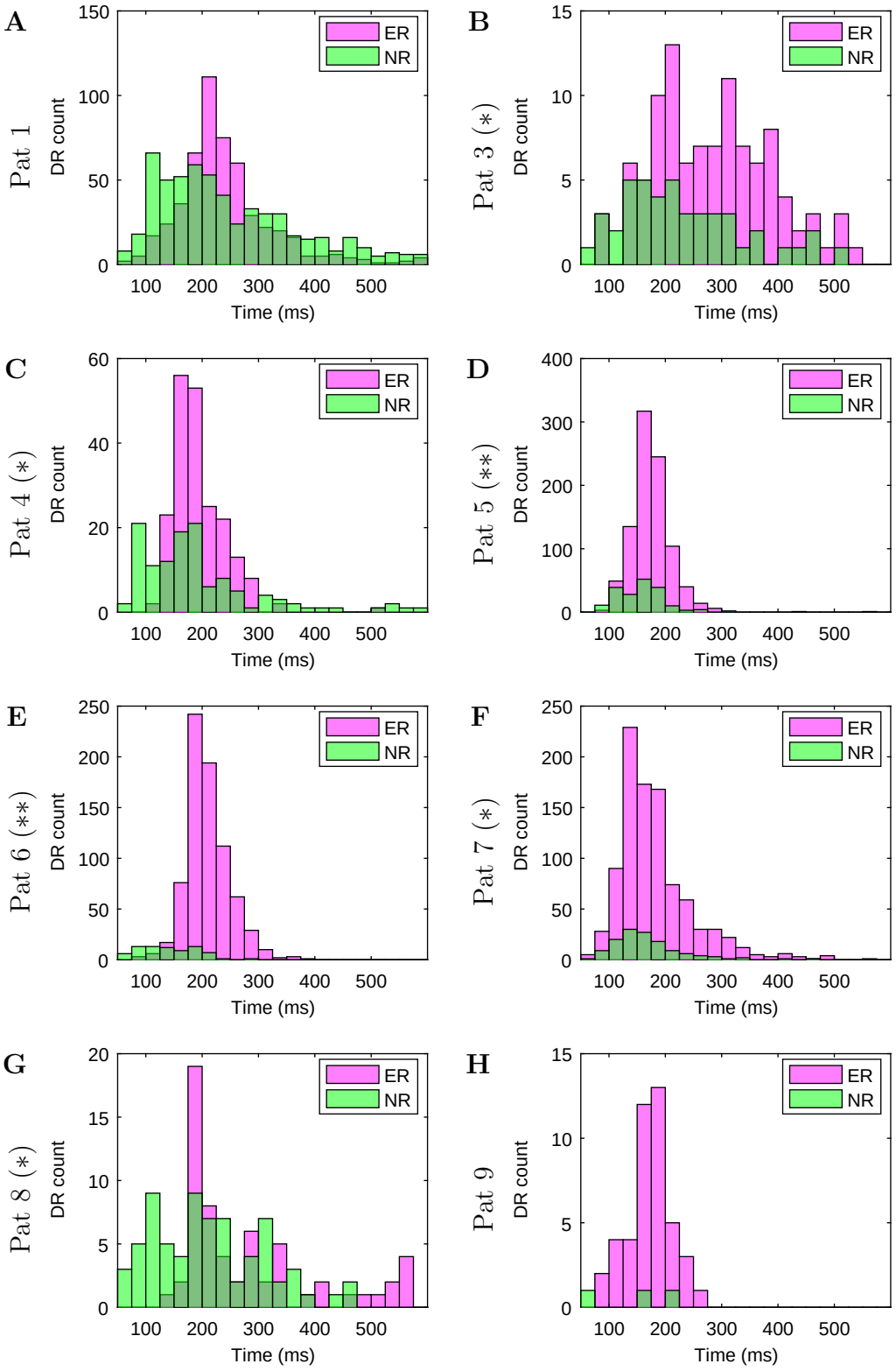

Figure 5: Distribution of onset times of delayed responses preceded by an ER (magenta) and delayed responses not preceded by an ER (green) for patients 1 and 3-9. Statistical significance results are indicated by $(*)$ and $(**)$ for $p < 0.05$ and $p < 0.001$, respectively.

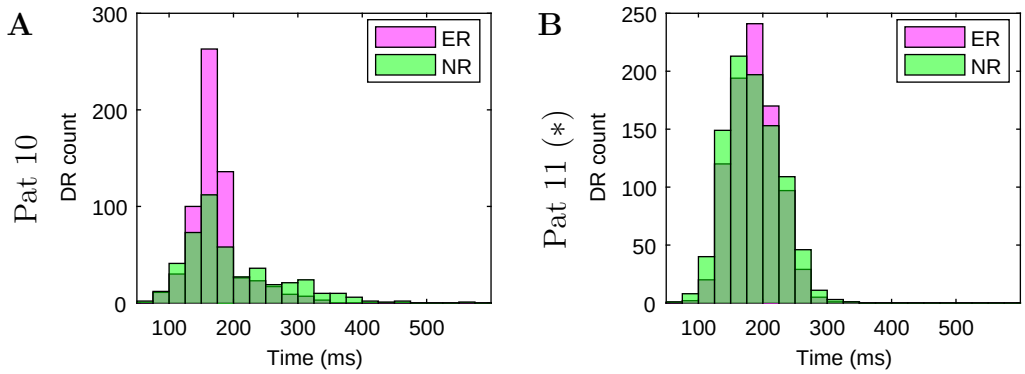

Figure 6: Distribution of onset times of delayed responses preceded by an ER (magenta) and delayed responses not preceded by an ER (green) for patients 10 and 11. Statistical significance results are indicated by $(*)$ and $(**)$ for $p < 0.05$ and $p < 0.001$, respectively.

References

[1] O. David, J. Bastin, S. Chabardès, L. Minotti, and P. Kahane. "Studying Network Mechanisms Using Intracranial Stimulation in Epileptic Patients". In: *Frontiers in Systems Neuroscience* 4 (2010), p. 148. DOI: 10.3389/fnsys.2010.00148.

[2] A. Dhooge, W. Govaerts, Y. A. Kuznetsov, H. G. E. Meijer, and B. Sautois. "New features of the software MatCont for bifurcation analysis of dynamical systems". In: *Mathematical and Computer Modelling of Dynamical Systems* 14.2 (2008), pp. 147–175. DOI: 10.1080/13873950701742754.

[3] A. J. Homburg and B. Sandstede. *Homoclinic and heteroclinic bifurcations in vector fields*. Vol. 3. Handbook of Dynamical Systems C. 2010, pp. 379–524.

[4] C. J. Keller, C. J. Honey, P. Mégevand, L. Entz, I. Ulbert, and A. D. Mehta. "Mapping human brain networks with cortico-cortical evoked potentials". In: *Philosophical Transactions of the Royal Society B: Biological Sciences* 369.1653 (2014). DOI: 10.1098/rstb.2013.0528.

[5] Y. A. Kuznetsov. *Elements of Applied Bifurcation Theory*. 3th. Springer, 2004.

[6] F. Wendling, F. Bartolomei, J. J. Bellanger, and P. Chauvel. "Epileptic fast activity can be explained by a model of impaired GABAergic dendritic inhibition". In: *European Journal of Neuroscience* 15.9 (2002), pp. 1499–1508. DOI: 10.1046/j.1460-9568.2002.01985.x.